Contents lists available at ScienceDirect

Applied Catalysis B: Environmental

Mesoporous TiO₂ modified with carbon quantum dots as a high-performance visible light photocatalyst

Ran Miao [a], Zhu Luo [b], Wei Zhong [b], Sheng-Yu Chen [a], Ting Jiang [c], Biswanath Dutta [a], Youmna Nasr [a], Yashan Zhang [a], Steven L. Suib [a,b,*]

[a] Department of Chemistry, U-3060, University of Connecticut, Storrs, CT 06269-3060, United States
[b] Institute of Materials Science, U-3136, University of Connecticut, Storrs, CT 06269, United States
[c] Department of Chemical and Biomolecular Engineering, University of Connecticut, Storrs, CT 06269, United States

ARTICLE INFO

ABSTRACT

We report a preparation method for visible light responsive Carbon Quantum Dots (CQDs) embedded in mesoporous TiO₂ materials. The as-prepared mesoporous TiO₂ (meso-Ti-450) material is a member of the recently designed University of Connecticut (UCT) mesoporous materials family. The UCT materials were synthesized based on sol-gel chemistry. The nanoparticles are randomly packed in inverse surfactant micelles and mesopores are formed by interconnected intraparticles. To achieve full usage of the visible region of sunlight (>400 nm), CQDs were introduced without destroying the mesopores. The photocatalytic performance of the CQDs/meso-Ti-450 was investigated by the degradation of methylene blue. Due to the up-conversion property and electron withdrawing property of CQDs, the photocatalytic activity of the composite material was largely enhanced under visible light irradiation. The highest photocatalytic activity was achieved by 5% CQDs/meso-Ti-450 in an hour. Compared to commercial P25, which is capable of removing 10% methylene blue (MB) under visible light conditions, the 5% CQDs/meso-Ti-450 can mostly remove MB (98%) under the same conditions. To date, the usage of mesoporous titanium oxide and carbon material composites for dye degradation under visible light has not been reported.

© 2016 Elsevier B.V. All rights reserved.

1. Introduction

Environmental and energy concerns have attracted significant attention on the development of highly efficient heterogeneous photocatalysts for the degradation of various kinds of organic contaminants [1–3]. Semiconductors have been widely studied as photocatalysts due to their wide absorbance range. Among the common semiconductors, such as iron oxide [4], copper oxide [5], and zinc oxide [6], titanium dioxide (TiO₂) has been widely studied and utilized in many photocatalytic applications. As a result of its long-term chemical and optical stability, strong oxidizing ability, nontoxicity, and low cost, TiO₂ is considered to be the most efficient photocatalyst to date [7]. The photocatalytic properties of TiO₂ are attributed to the production of photogenerated electrons in the conduction band (CB) and holes in the valence band (VB), which occur upon the radiation of ultraviolet (UV) light (10–400 nm). The photogenerated electrons and holes diffuse to the TiO₂ sur-

face and form highly reactive radicals (OH•, O₂•⁻), which are capable of oxidizing nearby organic molecules [8–11]. Among various TiO₂ materials reported, commercial TiO₂ (Degussa P25) is a benchmark photocatalyst and has been widely studied. P25 is a mixed phase TiO₂ material with 70–80% anatase and 30–20% rutile [12,13]. The remarkable photocatalytic efficiency contributes to the synergistic effect between anatase and rutile phases [14,15]. However, due to the relatively large band gap (3.0–3.2 eV), TiO₂ can only absorb short wavelength light, which falls in the UV region [16,17]. Given that the entire solar light consists of less than 5% ultraviolet light, the photocatalytic activity of TiO₂ under natural sunlight is largely limited [18]. In addition, commercial P25 is nonporous and has a relatively low surface area, which impedes the adsorption of target molecules, thus lowering the photocatalytic efficiency [19]. Therefore, the design of a high surface area and visible light responsive photocatalytic system has become an urgent task [16,20].

Mesoporous materials are considered as excellent catalysts for applications requiring high surface area and large amount of active sites, due to their tunable structural properties such as surface area, pore volume, size, and nanocrystallinity [21,22]. Mesoporous titanium dioxide that combines a photoactive framework and an open

* Corresponding author at: Department of Chemistry, U-3060, University of Connecticut, Storrs, Connecticut 06269-3060, United States.
E-mail address: steven.suib@uconn.edu (S.L. Suib).

porous structure is of great interest [23]. Mesoporous TiO_2 applied in the photocatalysis area has been extensively reported. Li et al. [24] synthesized gold nanoparticles embedded in a mesoporous titania photocatalyst and showed that gold nanoparticles are well dispersed in the mesoporous TiO_2 networks. The mesoporous channels offer a larger surface area and enhanced accessibility than P25. Feng et al. [25] reported that mesoporous titanium dioxide exhibits an enhanced photoreactivity relative to P25 due to the synergetic effects of the mesoporosity and light-transmittance ability of the catalysts. Zhu et al. [26] prepared flowerlike hierarchical TiO_2 materials with a high surface area and mesoporous channels, which exhibit good photocatalytic performance towards degradation of methylene blue. Both the mesoporous structure and unique morphology contributed to the enhanced activity compared to commercial TiO_2. However, the main drawbacks of conventional mesoporous TiO_2 materials are their poorly ordered mesoporous structure, low crystallinity, and low thermal stability. In 2013, our group has developed a general inverse micelle sol-gel approach for the preparation of a series of mesoporous metal oxide materials, which are called UCT materials (University of Connecticut mesoporous materials) [27]. The inverse micelle sol-gel method used Pluronic P123 as a surfactant species, which formed inverse micelles in a low pH condition. The presence of nitrate ions facilitates the penetration of positively charged metal nitro-clusters into the inverse micelle followed by a thermal decomposition of nitrate ions into nitric oxide species, which controlled the sol-gel chemistry. The 1-butanol, which served as an interface modifier and solvent, further prevented the undesirable aggregation. The subsequent calcination treatment generates thermally stable and crystalline mesoporous materials with monomodal and tunable pore sizes. The UCT materials have been used in various applications, such as photocatalytic reactions [28], water oxidation [29], methane oxidation [30], and CO oxidation [31]. Based on the inverse micelle sol-gel process, mesoporous TiO_2 (UCT-62) has been synthesized in this study.

In an attempt to improve the visible light photocatalytic activity of metal oxides, carbon nano-species have been utilized as modifying materials recently [32–34]. In terms of photophysical properties, carbon quantum dots have been found to possess excellent up-conversion photoluminence (UCPL). Up-conversion is a process where lower-energy light (near-infrared or infrared) is converted to higher-energy light (ultraviolet or visible) through multiple photon absorption. That is usually achieved via the use of lanthanide, actinide ions, transition metals, and semiconductor quantum dots [35–38]. Compared to down-conversion materials, materials with an up-conversion property are less common and more versatile, which are able to utilize the visible spectrum of sunlight, resulting in an improved photocatalysis efficiency [39,40]. Due to their unique optical properties such as bright fluorescence and strong absorption, CQDs have received much interest. Compared to the traditional metallic quantum dots, which are limited in use due to environmental hazard issues [41,42], CQDs possess low toxicity, good biocompatibility, high photostability, high aqueous solubility, strong emission, high natural abundance, and also are an electron reservoir [39,43–46]. Therefore, CQDs have gradually become promising carbon nanomaterials. Considerable work has been done on photocatalytic dye degradation with quantum dot-based materials, but only a few researchers are using CQDs on mesoporous materials. Yu et al. [2] developed CQDs embedded in a mesoporous hematite complex photocatalyst, which led to a high degradation efficiency of 97% for MB with the assistance of H_2O_2 under visible light. The intimate contact between CQDs and mesoporous hematite facilitated the electron transfer, and thus inhibited the electron-hole recombination. However, this photocatalyst requires coexistence of a strong oxidizing agent during the photocatalytic tests.

The CQDs embedded in mesoporous TiO_2 composite photocatalytic systems have not been reported previously. In this work, we demonstrated the design of a CQDs/mesoporous TiO_2 (UCT-62) composite to exploit full usage of the visible spectrum of sunlight based on the up-conversion property of CQDs. The CQDs modified mesoporous TiO_2 maintained the pure anatase phase and mesoporous structure, and exhibited high adsorption capacity and excellent visible light photocatalytic activity under ambient conditions.

2. Experimental section

2.1. Chemicals

Titanium (IV) isopropoxide (≥97%). 1-Butanol (anhydrous, 99.8%), poly(ethylene glycol)-block-poly(propylene glycol)-block-poly(ethylene glycol) PEO_{20}-PPO_{70}-PEO_{20} (Pluronic P123), L-ascorbic acid were purchased from Sigma-Aldrich. Concentrated nitric acid (HNO_3, 68–70%) was purchased from J. T. Baker. All chemicals were used as received and used without further purification.

2.2. Preparation of Meso-Ti-X and CQDs/meso-Ti-X

The mesoporous TiO_2 was synthesized by the recently developed inverse micelle template sol-gel approach [27]. In a typical synthesis, 2.84 g (0.01 mol) of titanium isopropoxide was dissolved in a solution containing 7.0 g (0.094 mol) of 1-butanol, 1.0 g (0.016 mol) of HNO_3 and 1.0 g (1.72×10^{-4} mol) of P123 surfactant in a 150 mL beaker at room temperature (RT) under magnetic stirring to obtain a clear gel. The formed clear gel was placed in an oven heated at 120 °C for 4 h, followed by a heat treatment under air at 250, 350, 450, 550 °C for 4 h, respectively. The as-prepared sample was labeled as meso-Ti-X (X = 250, 350, 450, and 550), representing the calcination treatment temperature. The carbon quantum dots were synthesized by an ultrasonic-hydrothermal method. L-Ascorbic acid was used as the carbon source. L-Ascorbic acid (1.0 g) was dissolved in a mixture of deionized water and anhydrous ethanol and treated ultrasonically for 2 h. Then, the obtained clear solution was transferred to a Teflon-lined stainless steel autoclave with a volume of about 23 mL, sealed and maintained at 160 °C for 4 h. The reaction mixture was then cooled to room temperature and extracted with dichloromethane. The water phase solution was collected and dialyzed. The above samples were labeled CQDs. Subsequently, 0.2 g meso-Ti-450 was dispersed in a suitable amount of CQDs solution. After continuous stirring the mixture for 30 min, the resulting mixture was washed with water, and dried in a vacuum oven at 80 °C to produce the CQDs/meso-Ti-450 composites. CQDs/meso-Ti-450 composites with different CQDs loading amounts were fabricated by adjusting the as-prepared CQDs amount.

2.3. Characterization of Meso-Ti-450 and CQDs/meso-Ti-450

All the synthesized materials were ground to a fine powder in an agate mortar. The Powder X-ray diffraction (XRD) analysis was carried out at room temperature on a Rigaku Ultima IV diffractometer (CuKα radiation, λ = 1.5406 A). A beam voltage of 40 kV and a current of 44 mA were used. The morphologies of the CQDs/meso-Ti-450 materials were investigated using an FEI Nova NanoSEM 450 with an accelerating voltage of 2.0 kV. Transmission electron microscopy (TEM) and high-resolution transmission electron microscopy (HRTEM) images were collected using a JEOL 2010 UHR FasTEM microscope operating at 200 kV. Fluorescence spectra were collected on an Agilent Cary 50 Eclipse fluorescence spectrophotometer using a 1.0 cm quartz cuvette. The excitation
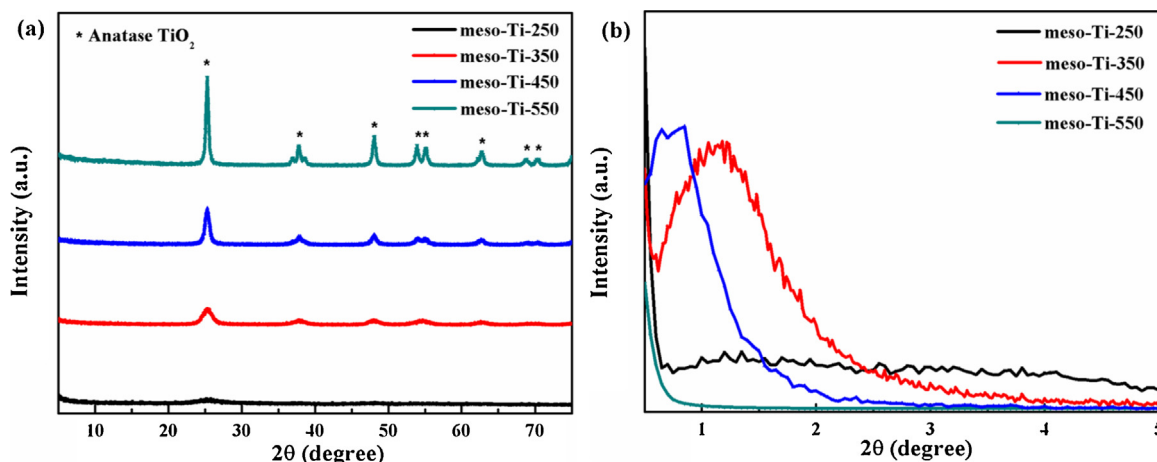
Fig. 1. (a) Wide angle and (b) low angle XRD patterns of meso-Ti-X (X = 250, 350, 450 and 550).

wavelength was set in the range of 350–750 nm N$_2$ sorption measurements were performed on a Quantachrome Autosorb-1-1C automated sorption system. The samples were degassed at 150 °C for 4 h prior to the experiments. The surface areas were calculated by the Brunauer–Emmett–Teller (BET) method, and the pore size distributions were obtained by the Barrett–Joyner–Halenda (BJH) method from the desorption branch of the isotherms. The thermogravimetric analysis (TGA) was performed using a Hi-Res TA instrument Model Q100, in the temperature range between 25 and 800 °C at a ramping rate of 10 °C min^{-1} in an air atmosphere. Raman spectra were taken on a Renishaw 2000 Raman microscope with an Ar$^+$ ion laser (514 nm) as the excitation source. Diffuse reflectance ultraviolet-visible (DR UV–vis) spectra of the powder samples were obtained with a diffuse reflectance apparatus attached to a Shimadzu UV-2450 ultraviolet-visible spectrophotometer. The powder samples were diluted with barium sulfate in proportions of 10–1, and pressed into the sample holder. X-ray photoelectron spectroscopy (XPS) measurements were performed in a PHI model 590 spectrometer with multiprobes (AlKα radiation, λ = 1486.6 eV, operated at 250 W).

2.4. Photocatalytic activity under visible light irradiation

The adsorption capacity was first investigated by dispersing 50 mg of photocatalyst in 50 mL of MB dye solution (1×10^{-4} M) under dark conditions for 100 min. Adsorption capacity was calculated by the ratio of dye concentration after adsorption (C) to that before adsorption (C$_0$). The photocatalytic activity of CQDs/meso-Ti-450 was investigated based on the photocatalytic degradation of Methyl Blue (MB) and *N*-benzylideneaniline. Experiments were carried out in a Rayonet Model RPR-100 photochemical reactor. A magnetic stirrer was placed at the center of the photoreactor. A 1000 W halogen lamp with a cutoff filter (λ > 450 nm) was used as a constant, separate, and intense visible light source. The photoreactor was covered with aluminum foil to reduce the effect of interference by ambient light. For MB degradation, 50 mg of CQDs/meso-Ti-450 was dispersed in a 50 mL MB dye solution (1×10^{-4} M) in a 200 mL quartz beaker. For *N*-benzylideneaniline degradation, 50 mg of photocatalyst and 50 mL 20 ppm of *N*-benzylideneaniline aqueous solution were applied. After 1 h of vigorous stirring in the dark, the solution was transferred with a magnetic stirrer inside the photochemical reactor, and the visible light lamps were turned on. The dye solution containing photocatalyst was kept stirring under irradiation for 2 or 3 h. A 3 mL sample solution was collected every 20 min. After removing the

photocatalyst with centrifuging, the clear solution was analyzed in a UV–vis spectrometer. Dye degradation efficiency was calculated by the ratio of absorbance intensity (I/I$_0$, where I and I$_0$ are the final and initial absorbance intensity, respectively). For MB degradation, calculations were based on the absorbance intensity of the 665 nm peak. For *N*-benzylideneaniline, calculations were based on intensity of the 252 nm absorbance. After the dye degradation tests, the photocatalysts were collected and washed with ethanol several times until methylene blue molecules desorbed back into solution. Then the photocatalyst powder was dried at 80 °C overnight. The subsequent recycle tests were carried out using the same photocatalytic reaction conditions as above. The stability test was conducted with the CQDs/meso-Ti-450 sample after the third recycle test by wide angle XRD techniques. To compare with the CQDs/meso-Ti-450, CQDs modified P25 material was prepared using the same method as CQDs/meso-Ti-450. The commercial P25 was used as received and without further treatment. The obtained sample was labeled as CQDs/P25. The photocatalytic degradation of MB was also performed in the absence of oxygen. The experimental procedure was the same as described above, except for purging nitrogen gas during the visible light irradiation to remove dissolved oxygen.

2.5. Analysis of intermediates and products

The intermediates formed during the dye degradation process were analyzed with an API 2000 mass spectrometer (Applied Biosystem/MDS SCIEX CA) using an electrospray ionization (ESI) source in a positive mode. A 1:1 ratio of HPLC-grade acetonitrile to dye solution was used. The CO$_2$ production analysis was carried out in a closed quartz dye degradation reactor with continuous flow (20 sccm) of compressed zero grade air, which contains a certain amount of CO$_2$. About 100 mg of CQDs/meso-Ti-450 photocatalyst was added into 100 mL MB (1×10^{-4} M) solution in the quartz reactor, and then the visible light lamps were turned on. The feed gas air was bubbled through the dye solution at a flow rate of 20 sccm. The outlet gas mixture was analyzed by an online gas chromatograph (SRI 8610C Multiple Gas Analyzer No. 1 GC) equipped with a thermal conductivity detector (TCD), a 6 ft long molecular sieve 13X packed column, and a 6 ft long silica gel packed column. About 1 cm^3 gas sample were injected every 20 min. Calculations were based on the ratio of CO$_2$ concentration in the gas sample (C) to the background feed gas (C$_0$).
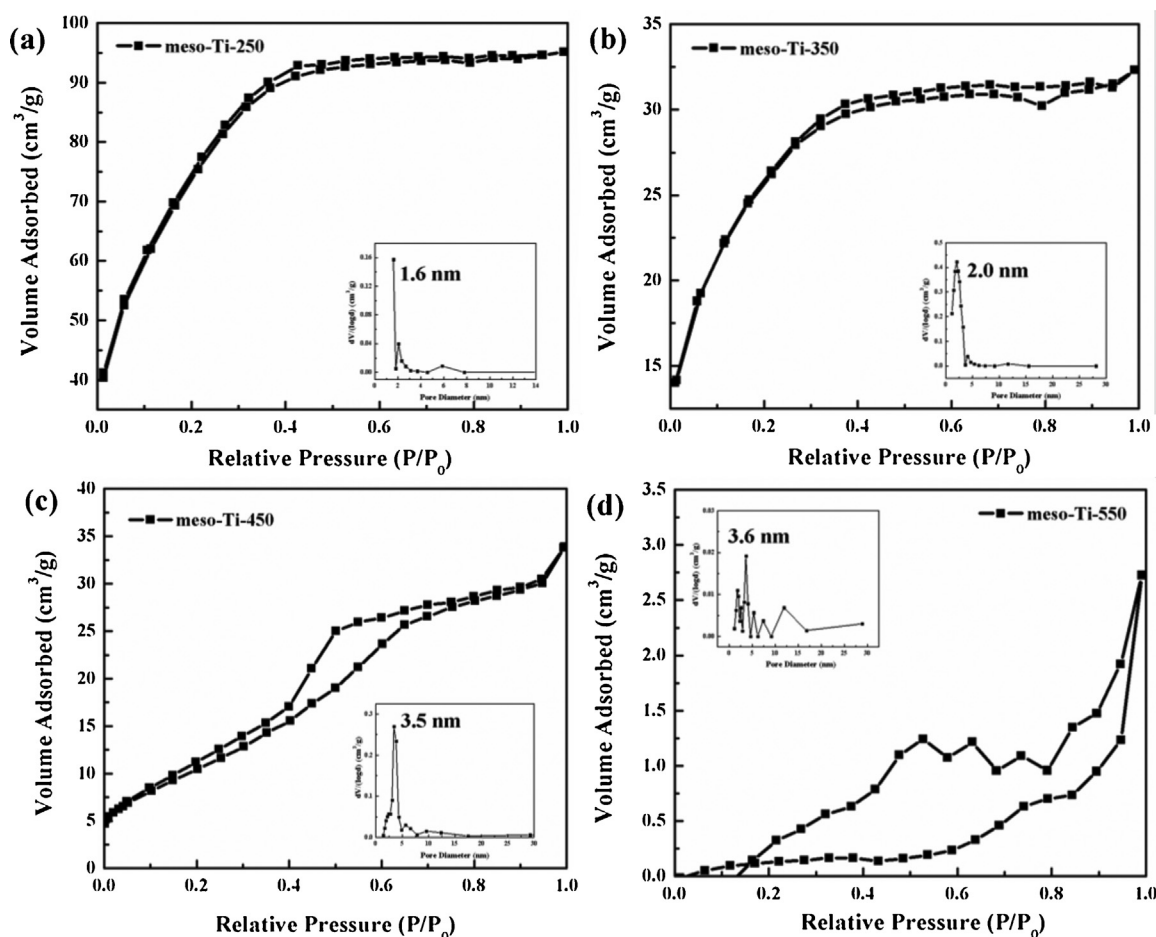
Fig. 2. N$_2$ sorption isotherms of (a) meso-Ti-250, (b) meso-Ti-350, (c) meso-Ti-450, and (d) meso-Ti-550. Inset: BJH desorption pore size distributions of each sample.

3. Results

3.1. Physiochemical properties of mesoporous TiO$_2$

Fig. 1 shows both the wide angle and low angle diffraction lines for titanium oxide materials calcined at different temperatures. All materials exhibit a typical anatase TiO$_2$ crystalline pattern according to JCPDS card (No. 00-021-1272). Increasing calcination temperature leads to a better crystallinity (Fig. 1a). The low angle diffraction peak is an indicator of a regular mesopore structure in soft-template prepared mesoporous materials. Since most mesoporous materials are amorphous on the atomic scale and process large unit cells, the diffraction angles are relatively small. Fig. 1b gives the low angle XRD patterns of titanium oxide materials. Meso-Ti-350 and meso-Ti-450 show a characteristic diffraction line in the low angle region, which reflects the existence of a mesoporous structure. Compared to meso-Ti-450, the low angle XRD diffraction line of meso-Ti-350 red shifted to a larger 2θ value, which can be explained by the particle size effect. According to the general trend in UCT materials, the pore expansion and particle size increase occurred when the heat treatment temperature increased. The lower angle position of the diffraction line for meso-Ti-450 indicated expanded pores and particles. When the heat treatment temperature was elevated above 450 °C, the low angle diffraction line was shifted to a lower angle. Meso-Ti-550 sample may preserve the mesoporous structure, but exceeds the detection limit of XRD. The mesoporous structure will be further confirmed by the N$_2$ sorption measurement.

To further confirm the trends shown in the low angle and high angle XRD patterns, N$_2$ sorption measurements were carried out. As shown in Fig. 2, only meso-Ti-450 exhibits a Type-IV adsorption isotherm, which indicates the presence of a mesoporous structure. The meso-Ti-250 shows its structure with a high surface area of 266 m^2/g, which is possibly due to the existence of surfactant. In order to examine the residue surfactant in each sample when different calcination temperatures are used, thermogravimetric analyses was performed. The meso-Ti-250 and meso-Ti-350 samples exhibit a total weight loss of 33% and 12%, respectively (Fig. S1). Similar to the results of N$_2$ sorption measurements, the TGA results show an incomplete removal of carboxyl and nitrate components in meso-Ti-250 and meso-Ti-350 samples. The existence of surfactant species and nitrate ions in residues will lead to a thermally unstable mesoporous structure [27], while both meso-Ti-450 and meso-Ti-550 samples present high thermal stability. Therefore, the surfactant species can be totally removed during calcination treatment above 450 °C. Along with increasing calcination temperature, the meso-Ti-450 demonstrates a pore size expansion (0.08 cc/g) and a large surface area (83 m^2/g). Fig. 2c shows a typical Type-IV N$_2$ sorption isotherm and BJH pore size distribution, suggesting a uniform mesoporous structure. Compared to meso-Ti-450, a drastic drop in surface area is observed for meso-Ti-550 samples. The loss of porosity at high treatment temperature confirms the tunable pore characteristics via heat treatments. Since only meso-Ti-450 exhibits good crystallinity, high thermal stability, and a mesoporous structure with characteristic type-IV adsorption isotherms, all the characterization and photocatalytic tests were performed

with CQDs/meso-Ti-450 samples. The detailed BET multipoint surface area, BJH desorption pore size distribution and pore volume of meso-Ti-X (X = 250, 350, 450 and 550) are displayed in Table S1.

3.2. Preparation and characterization of CQDs

Carbon quantum dots have been produced by many methods, such as electrochemical synthesis [47], laser ablation [48], reflux synthesis [49], hydrothermal synthesis [50], and microwave synthesis [51]. CQDs with unique fluorescent properties can be obtained by ultrasonic-hydrothermal treatment of L-ascorbic acid. This preparation method of CQDs has the merit of being environmentally friendly, facile, and lower cost than conventional preparation methods. The hydrothermal carbonization process required no strong acid, base, or organic solvent. Fig. 3a shows the TEM images of CQDs, which clearly express the well-dispersed nanoparticles with a near spherical-shaped morphology. The HRTEM image of the CQDs reveals the lattice spacing was around 0.32 nm, which corresponds to the (002) diffraction plane spacing of graphitic carbon. In the UV–vis spectra (Fig. 3b), the ultrasonic-hydrothermal synthesized CQDs exhibit a strong absorption peak around 260 nm, which indicated the typical absorption of aromatic π systems. In addition, the as-prepared carbon quantum dots showed broad absorption in the visible light region, which represented the high photocatalytic activities under visible light. In the inset picture (Fig. 3b, top right corner), two photographs of the CQDs aqueous solution under white light and UV light are shown. The bright blue fluorescence of CQDs is readily observed. Photoluminescence is one of the most attractive features of carbon quantum dots. To further explore the optical properties of the CQDs in aqueous solution, photoluminescence studies were carried out by using different excitation wavelengths. As shown in Fig. 3c, the PL spectra of carbon quantum dots are dependent on the excitation wavelength. When the excitation wavelength changes from 350 to 500 nm, the PL peaks shifted to a longer wavelength. The above result shows that the CQDs exhibit an excitation-dependent PL behavior. In addition to the strong down-conversion PL behavior, CQDs show a clear remarkable up-conversion property. Fig. 3d shows the PL spectra of CQDs excited by long wavelength light. The up-conversion PL shows the excitation-dependent PL behavior, similar to the down-conversion PL spectra. Along with increasing excitation wavelengths at 550, 600, 650, 700, and 750 nm, the up-converted emission peaks show a red shift with stronger intensity (from 355 to 525 nm). According to the previous reports about CQDs, the up-conversion property of CQDs should be ascribed to a two-photon absorption process [52,53]. As illustrated in Fig. 3e, when electrons in the π orbital are excited by low-energy photons, the photo-generated electrons would move to the high-energy state. Then, the excited electrons can fall back to the σ orbital by radiative relaxation. Thus, a shorter wavelength light is emitted [54].

3.3. Characterization of CQDs/meso-Ti-450 composites

Powder X-ray diffraction (XRD) was used to identify the phase of the products, crystal structure, and to determine the effect of CQDs on the crystallization of the TiO$_2$. Fig. 4a shows the XRD pattern of meso-Ti-450, the CQDs/meso-Ti-450 composite material, and the Joint Committee on Powder Diffraction Standards (JCPDS) pattern for anatase titania (JCPDS card No. 00-021-1272) as well. The CQDs/meso-Ti-450 composite was obtained via a hydrothermal method to achieve the deposition of CQDs on meso-Ti-450. As shown in Fig. 4a, CQDs/meso-Ti-450 composite shows the same characteristic diffraction lines of mesoporous TiO$_2$, which agree well with the standard pattern. Both materials display a pure anatase crystal structure. There is no additional carbon peak,

which indicates the small amount and high dispersion of CQDs in CQDs/meso-Ti-450 composite.

Raman and Fourier Transform Infrared Spectroscopy (FT-IR) studies were used to determine the graphitic component structure of the as-prepared CQDs and to investigate the functional groups present on the surface of CQDs/meso-Ti-450, respectively. Raman spectra of CQDs and CQDs/meso-Ti-450 samples are shown in Fig. 4b. The Raman spectrum of the CQDs sample shows no Raman signal under our measurement conditions, which is due to the strong fluorescence background of CQDs [55]. However, two bands at 1310 and 1620 cm^{-1} were detected for the CQDs/meso-Ti-450 sample, which can be attributed to the D and G bands of carbon, respectively. This observation indicates the strong fluorescence of CQDs in the CQDs/meso-Ti-450 composite quenched by TiO$_2$. The Raman spectra serve as further proof of a firm combination of CQDs with meso-Ti-450. The infrared spectra of meso-Ti-450 and CQDs/meso-Ti-450 are shown in Fig. 4b. The band around 1625 cm^{-1} and the band over the range 3200–3600 cm^{-1} present in both meso-Ti-450 and CQDs/meso-Ti-450 composites are due to the presence of surface adsorbed water molecules. The absorption band around 1380 cm^{-1} is associated with the vibration of the C—O—C group. The band around 1690 cm^{-1} corresponds to the C=C stretch, while the band located at 1750 cm^{-1} indicates the presence of C=O groups [2,5,44,51,55–57].

Since CQDs were not observed in the XRD pattern, TEM and HRTEM were carried out to further characterize the CQDs/meso-Ti-450 composites. Fig. 5a and b were collected from the bare meso-Ti-450 prepared by a sol-gel method, while Fig. 5c and d were collected from the 5% CQDs/meso-Ti-450. In Fig. 5a, the domain exhibits relatively small nanoparticles with a mean size of 10 nm. The mesopores are evenly dispersed among particles. Fig. 5c shows the high magnification HRTEM image of meso-Ti-450. They possess the anatase phase, with a lattice spacing of 0.35 nm, which agrees well with the (101) planes of the anatase phase. With the CQDs introduced into the system, the CQDs/meso-Ti-450 maintains a mesoporous structure. The mesoporosity of the composite materials was confirmed by N$_2$ sorption measurements (Fig. 6) and low angle XRD (Fig. 1b). As shown in Fig. 5b, the composite materials also consist of an anatase phase with the CQDs deposited on the surface of TiO$_2$. In Fig. 5**d**, the high magnification HRTEM image of CQDs/meso-Ti-450 shows the lattice spacing of 0.24 nm, corresponding to the (100) planes of graphitic carbon. The above results confirm the successful deposition of CQDs on the surface of meso-Ti-450 nanoparticles. The surface area and pore size distribution of meso-Ti-450 and CQDs/meso-Ti-450 samples were determined by N$_2$ sorption measurements. Fig. 6 shows N$_2$ sorption isotherms along with the BJH pore size distributions. Meso-Ti-450 has a surface area of 83 m^2/g and CQDs/meso-Ti-450 has a surface area of 53 m^2/g. The decrease in surface area may indicate the adsorption of CQDs inside the mesopores. This might also be due to the partial loss of mesoporosity. As shown in Fig. 6a and b, both isotherms show Type IV adsorption isotherms and a H$_2$-type hysteresis loop, according to the 1985 IUPAC classification [58], which confirms the presence of regular capillary pores [59]. The BJH desorption pore size distributions are presented in the insets of Fig. 6. The narrow pore size distributions were found to be 3.5 nm for meso-Ti-450 and 3.4 nm for CQDs/meso-Ti-450. The above results suggest the mesoporous structure was preserved with the introduction of CQDs. The composite material exhibits an open mesoporous structure, which may provide more active sites for the adsorption of organic molecules. XPS was used to investigate the chemical compositions and surface properties of the as prepared CQDs/meso-Ti-450 composite. Fig. 7 shows the full survey spectrum and narrow scan XPS patterns for the CQDs/meso-Ti-450 composite. The wide survey spectrum (Fig. 7a) verified the existence of titanium (Ti 2p), carbon (C 1s), and oxygen (O 1s) in the CQDs/meso-Ti-450 composite.
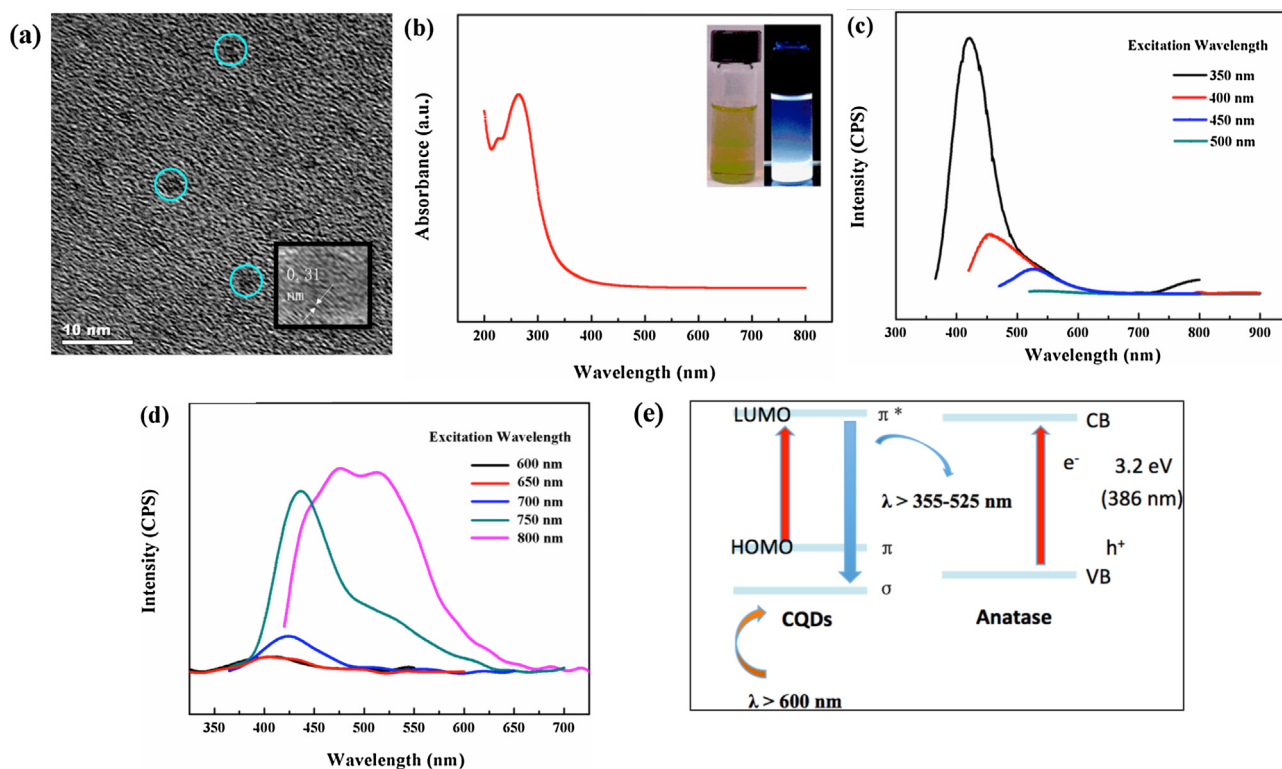
Fig. 3. (a) TEM images of as-prepared CQDs. (b) UV–vis absorption spectrum of the CQDs in aqueous solution. Inset: CQDs dispersed in water illuminated under white light (left) and UV light (right). (c) Down converted PL spectra of CQDs. (d) Up-converted PL spectra of CQDs. (e) Schematic illustration of electronic transition of CQDs.
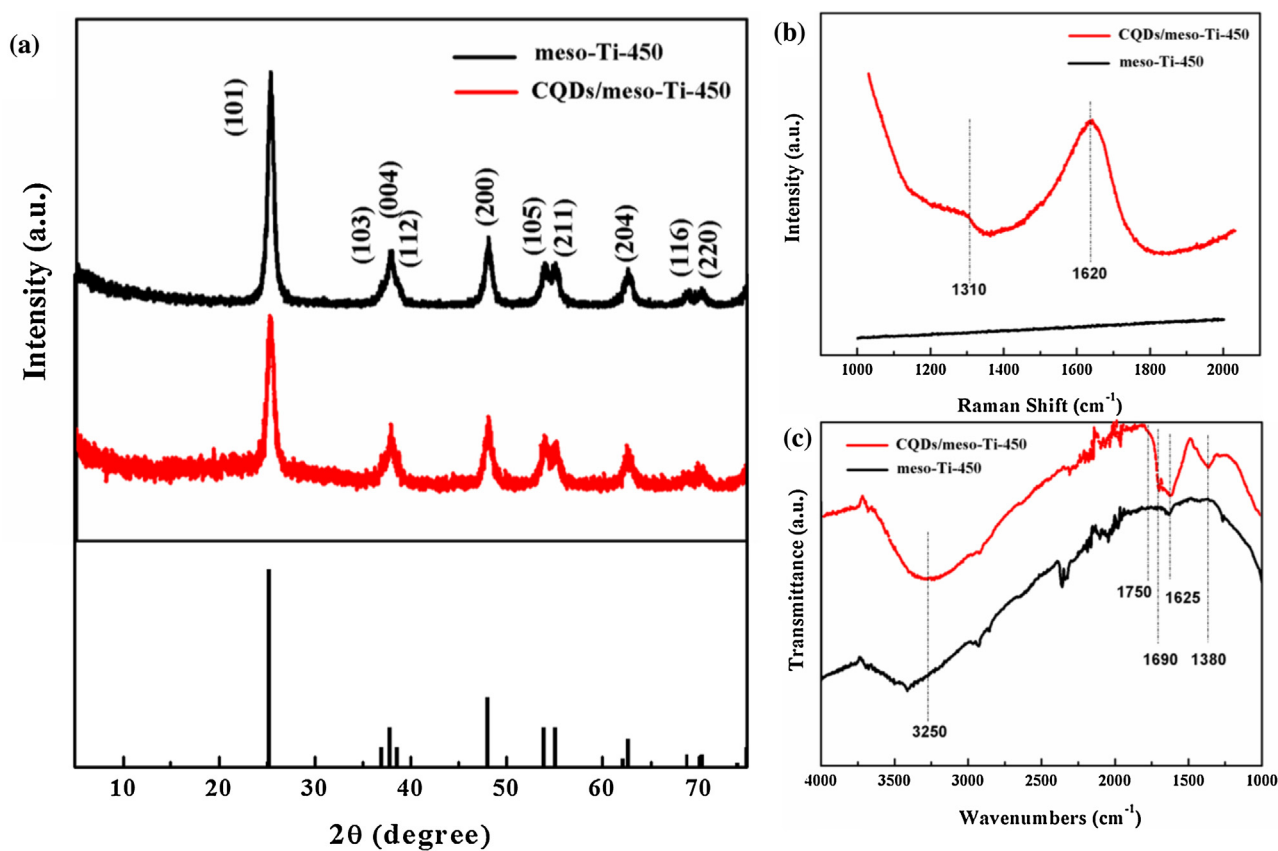

Fig. 4. (a) XRD patterns of pure meso-Ti-450, CQDs/meso-Ti-450, and the JCPDS pattern for standard Anatase. (b) Raman spectra of CQDs and CQDs/meso-Ti-450. (c) FT-IR spectra of meso-Ti-450 and CQDs/meso-Ti-450.
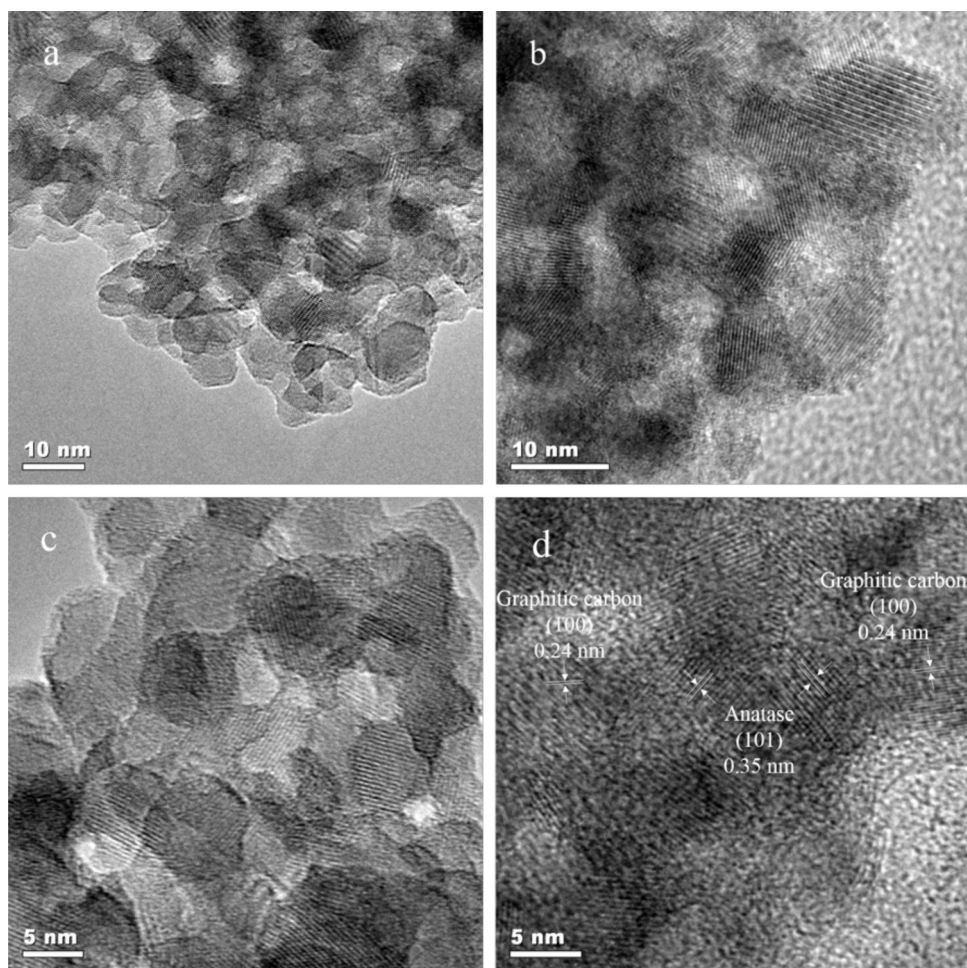
Fig. 5. Low magnification HRTEM images of (a) meso-Ti-450, (b) CQDs/meso-Ti-450 composites, and high magnification HRTEM images of (c) meso-Ti-450, (d) CQDs/meso-Ti-450 composites.
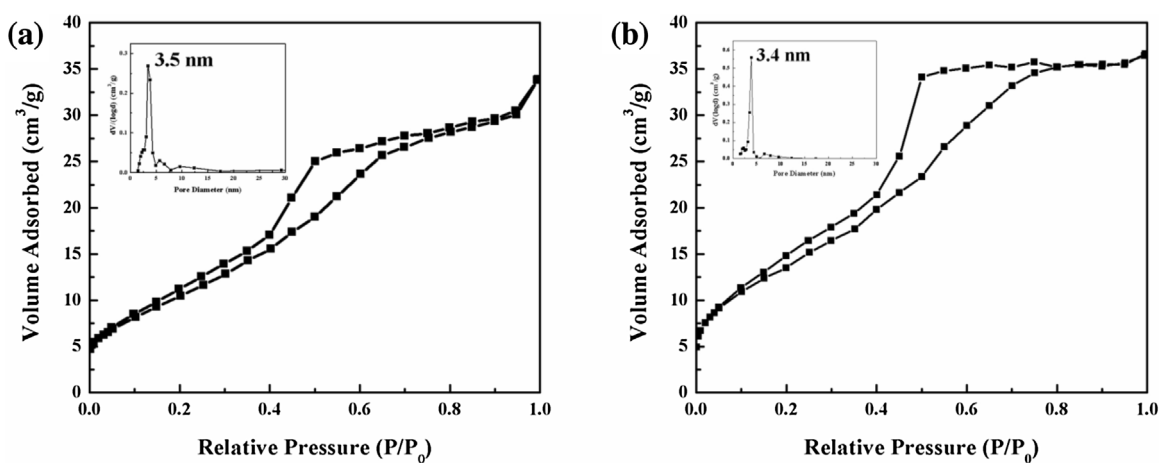

Fig. 6. Nitrogen adsorption-desorption isotherms for (a) meso-Ti-450, (b) CQDs/meso-Ti-450, and the corresponding BJH desorption pore size distributions curve.

The Ti 2p spectrum (Fig. 7b) was fitted to two peaks at 458.2 and 464.3 eV, which correspond to the 2p$_{3/2}$ and 2p$_{1/2}$, respectively. The spin energy separation of 6.1 eV was attributed to spin-orbital coupling. In the narrow scan of the C 1s (Fig. 7c), the deconvoluted XPS peaks of the C 1s at 283.9, 286.0, and 288.4 eV were assigned to the sp^2 hybridized carbons, sp^3 hybridized carbons, C=O and C=C—OH, respectively. The expanded pattern of O 1s is shown in Fig. 7d. The

broad peak was deconvoluted into four peaks. The peaks at 528.9, 530.8, 532.5, and 534.2 eV are ascribed to Ti = O, C=O, O=C—OH, and O—C—O, respectively [2,45,60]. Both the C 1s and O 1s XPS patterns show the presence of carbon-oxygen bonds in CQDs/meso-Ti-450 composites, which agrees well with the FT-IR spectroscopy results (Fig. 5b) indicating the presence of surface passivation groups on the surface of as-prepared CQDs/meso-Ti-450.
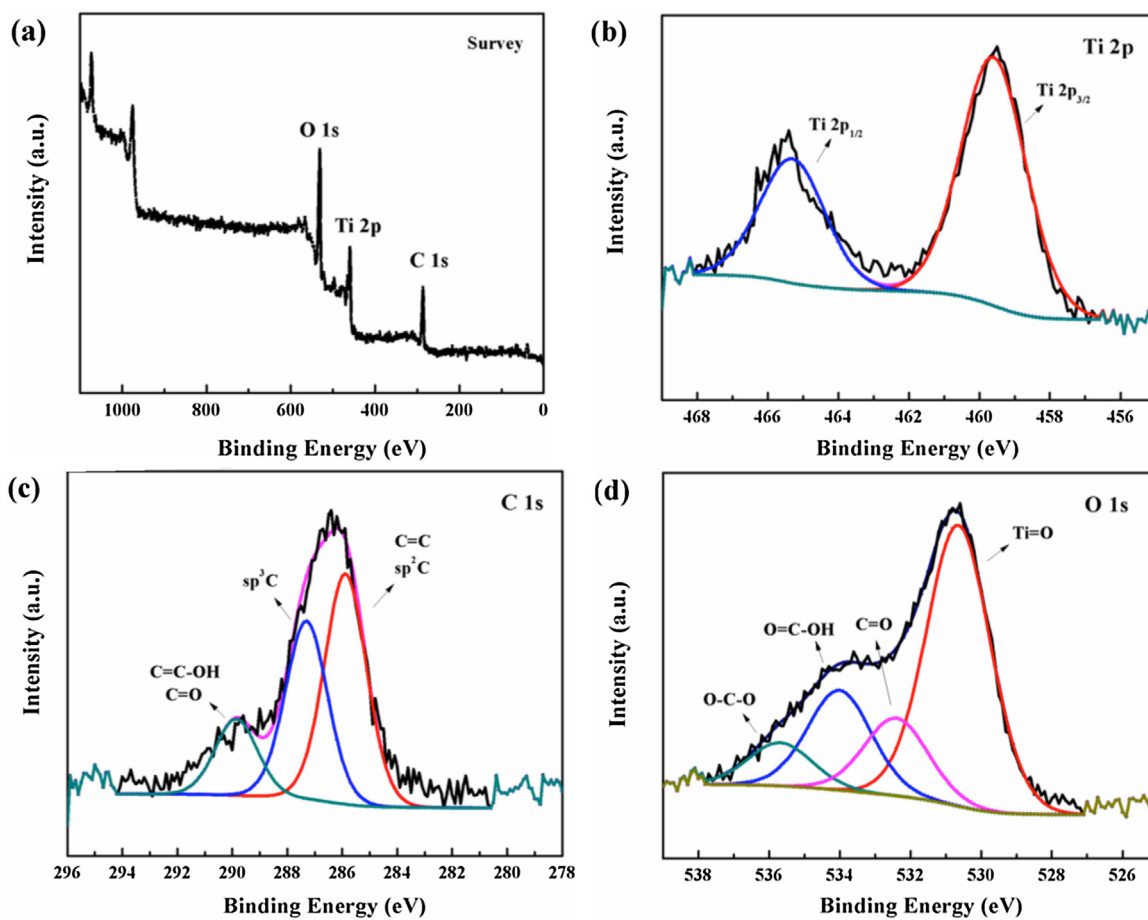
Fig. 7. X-ray photoelectron spectroscopy (XPS) patterns for CQDs/meso-Ti-450 composite.

3.4. Photocatalytic dye degradation under visible light irradiation

For a photocatalyst, the absorption range of sunlight plays a crucial role in the photoinduced dye degradation. In order to study the relationship between light absorption range and CQDs introduction into the meso-Ti-450, diffuse reflectance spectra (DRS) measurements of the CQDs/meso-Ti-450 composite were carried out. Pure anatase phase has a larger band gap (3.2 eV), which makes the material more transparent in the visible light region, and hence exhibits lower photocatalytic activity under visible light irradiation [61]. As shown in Fig. S2a, meso-Ti-450 shows no absorption in the visible region of 410–800 nm, which agrees well with the absorption ability of mesoporous TiO_2. Fig. S2b and S2c present the color changes of TiO_2 before and after addition of CQDs. The CQDs/meso-Ti-450 composite powder shows a brownish color, which indicates its ability to absorb visible light. Compared to the bare meso-Ti-450, CQDs/meso-Ti-450 exhibits an obvious red shift, and remarkable absorption in the visible light region. The result demonstrated that the CQDs/meso-Ti-450 composites may exhibit a narrowed band gap compared to that of meso-Ti-450 due to the addition of CQDs. As a result of the extended absorption range, the photocatalytic ability of CQDs/meso-Ti-450 showed a great enhancement, due to a better utilization of visible light. To value the synergistic effect between CQDs and mesoporous TiO_2, the CQDs modified P25 material is prepared for comparison. Compared to the obvious extended absorption range of CQDs/meso-Ti-450, the absorption range of P25 barely shows an extension after the addition of CQDs, which is probably due to the nonporous nature of P25 (Fig. S3). In order to further confirm the synergistic effect, CQDs modified P25 has been prepared and used as photocatalyst in the degradation of MB.

Compared to the CQDs/meso-Ti-450, CQDs/P25 exhibits less dye adsorption capacity within 1 h adsorption in the dark. When we transferred the dye solution contained CQDs/P25 photocatalyst into a photochemical reactor for dye degradation tests, there was about 40% degradation of MB observed by CQDs/P25 photocatalysts. The above results are in accordance with the diffuse reflectance spectra (DRS) measurement results (Fig. S3).

The photocatalytic activity of as-prepared CQDs/meso-Ti-450 composites was studied via photocatalytic degradation of Methylene Blue (MB) under visible light irradiation. Prior to the dye degradation studies, the adsorption ability tests were carried out under dark conditions. P25 and CQDs barely show adsorption ability, while meso-Ti-450 and CQDs/meso-Ti-450 composites exhibit fair adsorption capacities. Compared to CQDs/meso-Ti-450 composites, the adsorption efficiency of meso-Ti-450 is higher (Fig. 8a). The relatively low adsorption capacity of CQDs/meso-Ti-450 composites is due to the contracted pore size as the CQDs are filling inside the mesopores. The results are well in accordance with the N_2 sorption results (Fig. 6). When visible light and a very high starting concentration of methylene blue were used (32 mg/L), the CQDs/meso-Ti-450 exhibited excellent photocatalytic efficiency. The relationship between concentration of MB solution and visible light irradiation time is shown in Fig. 8b. As can be seen, the photo-induced dye degradation efficiency is up to 98% in 1 h with as-prepared CQDs/meso-Ti-450 as the photocatalyst. For comparison, commercial P25, pure meso-Ti-450, and pure CQDs aqueous solution were used as photocatalysts in the contrast experiments. There is less than 5% degradation of MB observed, which confirmed the enhanced visible light response of CQDs modified mesoporous TiO_2. The remarkable photocatalytic activity of CQDs/meso-Ti-450
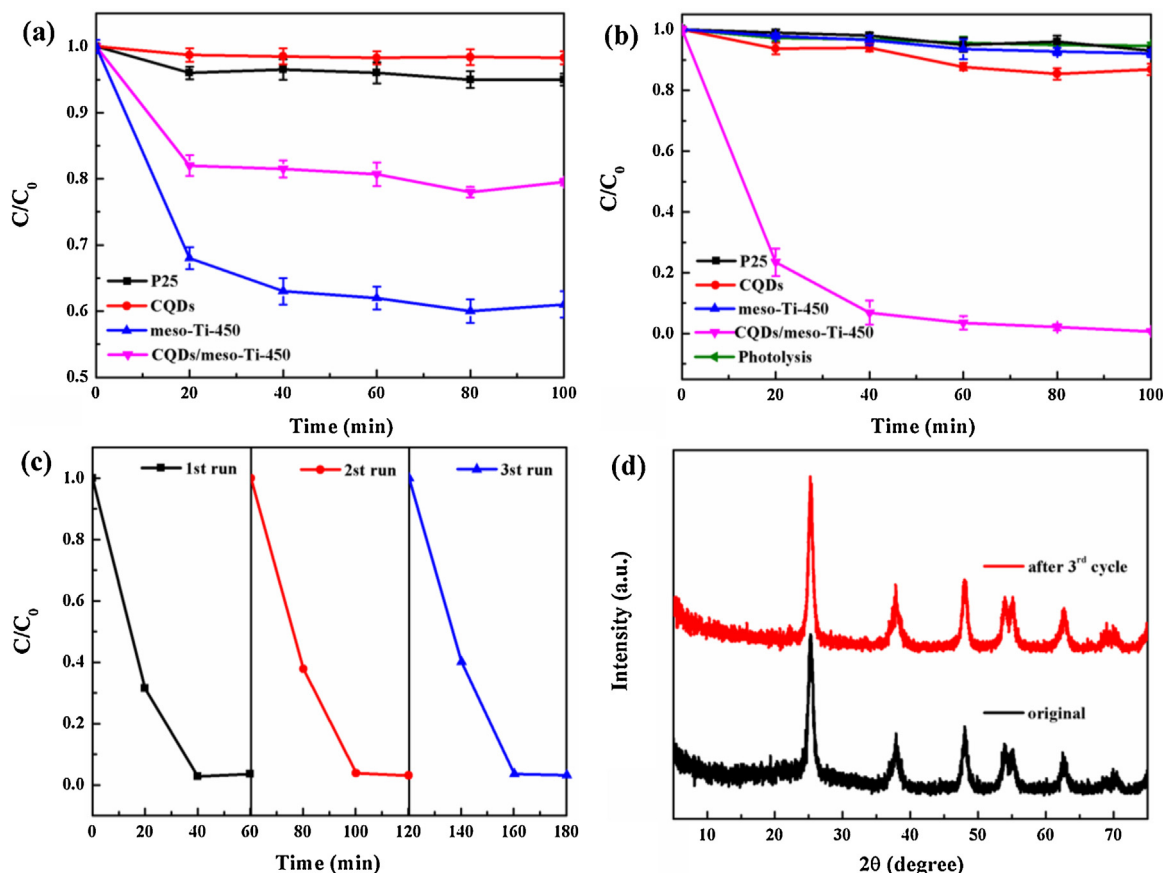
Fig. 8. (a) Adsorption efficiency tests for P25, CQDs, meso-Ti-450, and CQDs/meso-Ti-450 by dispersing 50 mg each sample in 50 mL, 1×10^{-4} M MB dye aqueous solution under dark conditions. (b) Photocatalytic degradation of 50 mL, 1×10^{-4} M MB dye aqueous solution under visible light in 100 min by using 50 mg of P25, CQDs, meso-Ti-450, CQDs/meso-Ti-450, and blank control without any photocatalyst (photolysis), respectively. (c) Recycle performance test of CQDs/meso-Ti-450 sample. (d) Wide angle XRD patterns of CQDs/meso-Ti-450 sample before and after recycle performance test.

can be ascribed to the interaction between CQDs and meso-Ti-450. In order to test the recycling ability and stability of CQDs/meso-Ti-450, the photocatalyst was collected after degradation reaction, and washed by deionized water. Then the sample was dried at 100 °C in an oven overnight. The recovered photocatalyst was used for recycle tests. Fig. 8c shows the photocatalytic performance of CQDs/meso-Ti-450 for three cycles in dye degradation tests. The photocatalyst exhibits repeatable catalytic activity during three cycles with only a slight decrease. In the wide angle XRD patterns of CQDs/meso-Ti-450 sample before and after three cycles, no obvious change in characteristic lines was observed (Fig. 8d). The above results demonstrated the good recyclability and stability of the composite material.

To further explore the photocatalytic activity of the CQDs modified meso-Ti-450, the effect of loading amount of CQDs was investigated. Notably, the loading amount of CQDs in the present system can largely affect the dye degradation efficiency. As shown in Fig. S5, the photocatalytic degradation efficiency is the highest (about 90% degradation in 40 min) when 5% (weight percent) CQDs was added into the system. However, further increasing the loading amount of CQDs decreases the dye degradation efficiency to 60%. This indicates that the capacity of mesopores on the surface of meso-Ti-450 correlates with the loading amount of CQDs. The excessive CQDs can impede the reaction of photo-generated electrons and holes with surface adsorbed oxidants and reducers [62]. Another factor to consider is the inner filter effect, which occurred due to a high concentration of fluorescent molecules, CQDs in this case. In the presence of highly concentrated CQDs,

the excitation energy or emission energy will be absorbed by CQDs themselves and resulted in lower energy reached onto the CQDs/meso-Ti-450 composite. Proper control of the quantity of the absorbing fluorophore molecules is important to the photocatalytic activity. The actual content of CQDs in the CQDs/meso-Ti-450 composites was further confirmed by thermogravimetric analysis (TGA). As shown in Fig. S6, compared to that of the pure mesoporous TiO$_2$, the CQDs/meso-Ti-450 materials show a greater overall weight loss. The meso-Ti-450 has a total weight loss (ca. 0.8 wt%) between 50 and 200 °C, which is due to desorption of physisorbed water molecules on the surface of the materials and the loss of water molecules that were chemically bonded in the mesoporous structure. The TGA curves of 5% CQDs/meso-Ti-450, 10% CQDs/meso-Ti-450, 15% CQDs/meso-Ti-450 show a 4.1, 6.2, and 15.1 wt% total weight loss, respectively. The first weight loss was observed between 50 and 200 °C, which was attributed to the loss of water molecules. The second weight loss occurred between 250 and 400 °C, which was ascribed to the combustion of the carbon source. The second weight loss increases with an increase in the loading amount of CQDs in the composites. This second weight loss correlated with a different initial loading amount of CQDs in mesoporous TiO$_2$ (5%, 10%, 15%, respectively). The 15% CQDs/meso-Ti-450 showed the largest weight loss, while pure meso-Ti-450 exhibited the smallest weight loss. These features indicated the successful introduction of different loading amounts in CQDs, and confirmed the actual content of CQDs in the composites.

Fig. S7 displays the color change of methylene blue solution before and after the photo-

catalytic test. Before the start of irradiation, the methylene blue solution containing the photocatalyst was placed under dark conditions for 2 h to reach adsorption-desorption equilibria. As shown in Fig. S7, there is a vague color change from deep blue to light blue, which indicated the adsorption ability of CQDs/meso-Ti-450. After the visible light was turned on, the methylene blue solution was changed from light blue to a colorless solution within 80 min under ambient conditions. The dye degradation mechanism was further investigated by intermediate analysis using Electrospray Ionization Mass Spectrometry and CO_2 evolution.

The main intermediates formed during irradiation of Methylene Blue under visible light were qualitatively identified via ESI/MS. The 5% CQDs/meso-Ti-450 sample was used in the intermediate analysis. At 0 min of the degradation reaction, the ESI–MS spectrum (Fig. S8a) showed the main strong peak at $m/z = 284.2$, which belongs to the pure Methylene Blue parent molecule (see structure in Fig. S10). Upon addition of as-prepared CQDs/meso-Ti-450 sample into the dye solution under visible irradiation, the peak at $m/z = 284.2$ disappeared, along with several new peaks at $m/z = 268.2, 252.2, 225.0, 196.0,$ and 153.1 of intermediates started to appear (Fig. S8b). The samples for analysis were collected in the middle of the degradation (20–30 min). A possible mechanistic pathway of degradation was developed in Fig. S8b. The new peaks appearing at $m/z = 268.2$ and 252.2 suggest the process of demethylation, while the peaks at 225.0 and 196.0 indicate the N-demethylation. In addition, the spectrum shows a peak at a lower mass ($m/z = 153.1$), suggesting the demethylation occurs with the cleavage of the ring. The ESI results suggest degradation should be the major mechanism instead of adsorption. In order to confirm that the dye molecules are adsorbed onto the photocatalyst instead of degradation under dark conditions, the dye solution was collected after a 2 h adsorption test in the dark. Fig. S9 shows the ESI results for the MB solution after and before the adsorption test. The peak located at $m/z = 284.2$ displays a slightly decreased intensity. No new signal corresponding to intermediates was observed. Therefore, adsorption is likely to be the main mechanism under dark conditions.

In order to better understand the photocatalytic mechanism of CQDs modified mesoporous TiO_2, 5% CQDs/meso-Ti-450 was used as a photocatalyst in the degradation of colorless aromatic pollutants. N-Benzylideneaniline was chosen as a target organic molecule, because of its zero absorbance under visible light. Prior to the degradation study, the adsorption ability was first investigated. Fifty mg of catalyst dispersed in 50 mL of 20 ppm N-benzylideneaniline aqueous solution was applied in dark conditions for 1 h. The halogen lamp was turned on when the solution achieved adsorption equilibrium. As shown in Fig. S11, 30% of N-benzylideneaniline was degraded after 2 h. For comparison, degradation experiments of N-benzylideneaniline aqueous solution were carried out with P25 as the photocatalyst and without any catalyst, respectively. No significant degradation was observed. CQDs/meso-Ti-450 material not only can be used for dye degradation but also for colorless organic pollutants. Thus, we can conclude that the as-prepared photocatalyst can be excited by visible light without the presence of dye molecules. In other word, the dye-sensitized semiconductor mechanism can be excluded.

Photocatalytic activity in the absence of oxygen was also investigated to study the CQDs role in the photo-induced electron-hole separation. Nitrogen gas was purged during the dye degradation test to remove the dissolved oxygen. The dye degradation efficiency of CQDs/meso-TiO_2 photocatalyst under N_2 gas is shown in Fig. S12. No obvious degradation was observed for the pure mesoporous TiO_2. Under visible light irradiation, CQDs/meso-TiO_2 is able to remove about 38% of MB dye in 2 h.

To further investigate the photocatalytic activity of CQDs/meso-Ti-450, the production rate of CO_2 under visible light irradiation

of the as-prepared sample was measured. Fig. S13 shows the CO_2 production under atmospheric conditions. Without visible light irradiation, the background CO_2 concentration was stable (-20 to 0 min). After visible light was turned on (0 min), this led to a significantly increase in the concentration of CO_2 in the first 40 min. The remarkable CO_2 evolution indicates the total oxidation of MB molecules to CO_2 molecules. After 40 min, the reaction started to slow down due to the consumption of the photocatalyst and dye molecules. The CO_2 production occurs along with the dye degradation process. The as-synthesized CQDs/meso-Ti-450 composite is able to decompose MB molecules to intermediates, and further totally oxidize them to CO_2.

4. Discussion

In this study, the mesoporous TiO_2 was synthesized by a recently developed inverse micelle sol-gel method [27]. This approach involves sol-gel reactions of the transition metal oxo-clusters with surfactant species in hydrated inverse micelle nanoreactors. The reaction was controlled by the unique thermal decomposition of nitrate ions. The formed NO_x species are attached to metal oxo-clusters, followed by an increased acidity and the formation of mesoporous metal oxides [63]. The formed mesostructure of the meso-Ti-450 sample was confirmed by the N_2 sorption measurements (Fig. 2c), which showed typical Type IV adsorption isotherms. To further decorate the mesoporous TiO_2, mono-dispersed CQDs were added into the system. In comparison with mesoporous TiO_2, the CQDs modified meso-TiO_2 exhibits a decreased surface area and smaller pore size, which contributed to the CQDs being embedded into the mesopores and probably partial loss of mesoporosity. However, the presence of aromatic rings and oxygen containing groups of CQDs may contribute to the adsorption toward methylene blue and N-benzylideneaniline molecules on the photocatalyst composite via π-π conjugation. This process facilitates the photo-induced degradation of the adsorbed target molecules. The CQDs were prepared by an ultrasonic-hydrothermal method. The ultrasonic waves lead to aromatization of L-ascorbic acid followed by carbonization under hydrothermal treatment [64,65]. In order to explore the surface functional groups, the Raman spectrum of CQDs/meso-TiO_2 was collected. A weak D band and a strong G band were observed in the spectrum (Fig. 4b). As the intensity ratio of the D and G bands is an indicator of the disordered content of carbon and the ratio of the sp^3/sp^2 carbon components, abundant oxygenated sp^2 carbon groups are mainly occupied at the surface of the CQDs/meso-TiO_2 composite. The surface properties were further confirmed by XPS, which suggested the presence of surface hydroxyl and carboxyl groups (Fig. 7c). Other evidence related to the surface carbon components of the composite material involves the HRTEM images of as-prepared CQDs modified mesoporous TiO_2. As shown in Fig. 5d, the area exhibits relatively small particles embedded in the mesopores or attached on the surface of TiO_2. The small particles display a lattice spacing of 0.24 nm, which can be assigned to the (100) planes of the graphitic carbon. Based on the above results, the close contact between CQDs and mesoporous TiO_2 could be an advantage for the electron transfer process, thus the enhanced photocatalytic activity.

The adsorption capacity and photocatalytic performance of CQDs/meso-Ti-450 was investigated by dye degradation of MB under dark condition and visible light irradiation, respectively (Fig. 8a and b). The efficiency of photocatalysts is affected by various factors. In this study, both the mesoporous structure of CQDs/meso-Ti-450 and introduction of carbon quantum dots greatly contribute to the enhanced dye degradation efficiency. The unique mesoporous structure contributes a great deal to the photocatalytic activity of as-prepared materials. Since small organic molecules
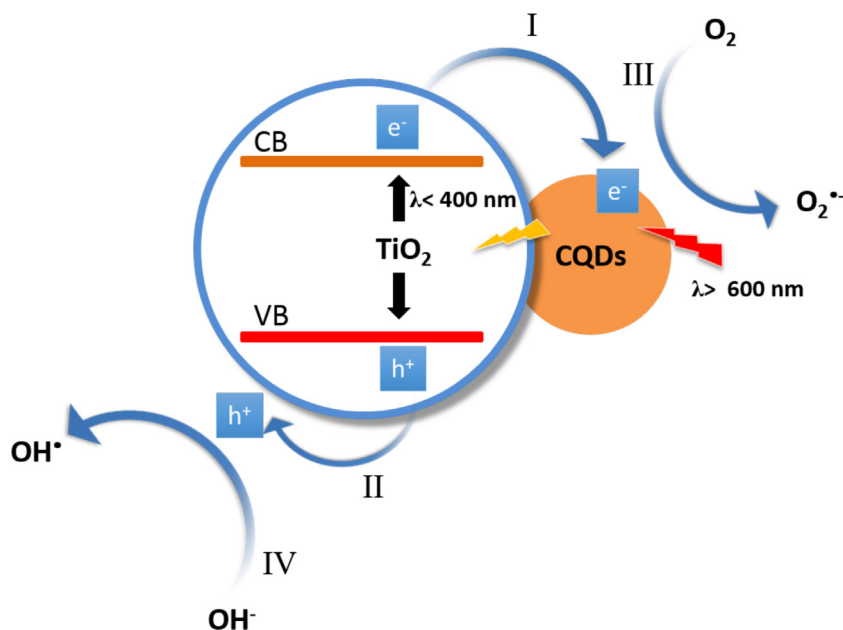
Scheme 1. Mechanism of the photocatalytic process for CQDs/meso-Ti-450 under visible light irradiation.

can be adsorbed into the pores more efficiently, adsorption is considered as a prerequisite for good photo-induced dye degradation activity [19]. In this reaction protocol, the mesoporous structure of TiO_2 acts as a substrate for CQDs nanoparticles. The open mesoporous structure and large surface area produced more active sites, which can facilitate the interaction between CQDs and mesoporous TiO_2 [2]. Thus, CQDs can act as active sites for adsorption of target molecules via the strong π-π conjugation. To confirm the important role of mesoporous TiO_2 in photocatalysis, CQDs modified nonporous commercial P25 is synthesized for comparison. However, compared to CQDs/meso-Ti-450, introduction of CQDs does not greatly alter the absorption band of P25 (Fig. S3). The corresponding dye degradation performance of CQDs/P25 is in accordance with the DRS results. Compared to CQDs/P25, the CQDs/meso-TiO_2 composite photocatalyst showed much higher degradation ability toward the MB dye (Fig. S4). Therefore, the mesoporous structure may play an important role in the high photocatalytic activity of the composite material. However, in this photocatalytic system, the CQDs modified meso-Ti-450 has lower adsorption efficiency than that of unmodified meso-Ti-450. The optical properties of CQDs are other key reasons for the high photocatalytic activity. CQDs have an attractive up-conversion photoluminescence property (Fig. 3d) in addition to the normal down-conversion photoluminescence. In a typical up-conversion fluorescence process, the emission photon energy is higher than that of the excitation. The possible mechanism is a multiple photon process [45,66,67]. Due to this unique property, CQDs can act as efficient energy converters. The CQDs first absorbed long-wavelength light ($\lambda > 600$ nm), followed by shorter wavelength light emission located in the range of UV light, which further excites TiO_2 to produce photogenerated electrons and holes (Scheme 1). In addition, CQDs existed as efficient electron reservoirs, which can trap electrons emitted from the conduction band of TiO_2 [68]. Thus, the electrons in the TiO_2 conduction band will transfer to the CQDs (process I), to further react with molecular oxygen to produce superoxide anion radicals ($O_2^{\bullet-}$) (process III). Meanwhile, the photogenerated holes in the valence band will migrate to the surface of TiO_2 (process II), and then react with hydroxyl species to form active hydroxyl radicals ($OH^{\bullet}$) (process

IV) [7,11,69]. Similar to the mechanism reported in the literature, those highly active radicals exhibit remarkable oxidizing ability to organic molecules adsorbed on the surface of TiO_2. Based on the proposed mechanism, the presence of CQDs can hinder the electron-hole recombination, and improve the photocatalytic efficiency. To confirm the role of CQDs as an electron scavenger, photocatalytic degradation of MB was conducted in a N_2 atmosphere. Since oxygen can work as a potential electron acceptor, we removed dissolved oxygen by purging with N_2 during the measurements [70]. Compared to mesoporous TiO_2, the CQDs modified TiO_2 exhibits higher degradation efficiency. This suggests CQDs prohibits the recombination process of photogenerated electrons and holes, by facilitating electrons migrating from the conduction band of TiO_2 to CQDs on the surface. However, N_2 saturation leads to a decreased photocatalytic efficiency overall, in comparison with the same photocatalytic reaction under ambient conditions. As shown in Fig. 8b, the MB dye can be mostly decomposed (98%) in the presence of CQDs/meso-Ti-450 in 1 h under visible light irradiation. The dye degradation performance is much superior to that of commercial P25 and unmodified meso-Ti-450. The degradation process has been further evidenced by ESI/MS measurements (**Fig. S8**). The peak at $m/z = 284.2$, which corresponds to the MB dye molecule, disappeared after visible light irradiation, which strongly suggests photo-induced degradation. Meanwhile, the appearance of new peaks with characteristic $m/z < 284.2$ implies the formation of small fragments of MB dye molecules. Those small fragments can be assigned as different intermediates and products produced in the process of $OH^{\bullet}$ and $O_2^{\bullet-}$ attack. Methylene blue dye molecules can work as photosensitizers to produce electrons, which are injected to the conduction band of TiO_2 [71,72]. In the present study, the colorless organic molecule, N-benzylideneaniline, can also be partially degraded by the composite photocatalyst (Fig. S11). We may exclude the dye sensitization mechanism and prove that the CQDs modified mesoporous TiO_2 can be excited by visible light without the presence of a dye. This agrees well with our proposed mechanism. In this study, the CQDs modified meso-Ti-450 shows much higher photocatalytic activity under visible light under ambient conditions.

5. Conclusions

In summary, CQDs embedded mesoporous TiO$_2$ composites were first successfully synthesized by a low cost, environmentally friendly sol-gel and ultrasonic-hydrothermal method. The mesoporous structure was preserved with the introduction of CQDs. The photocatalytic activity was investigated using methylene blue degradation under visible light irradiation. Compared to commercial Degussa P25, pure mesoporous TiO$_2$, and CQDs/P25, CQDs/meso-Ti-450 composites showed enhanced catalytic performance. The optimized composite (5% CQDs-meso-Ti-450) possessed a surface area of 53 m^2/g and a pore size of 3.4 nm. The composite exhibits the highest visible light induced photocatalytic activity toward methylene blue dye (up to 98% degradation efficiency in 1 h). Photocatalytic activity of 5% CQDs-meso-Ti-450 was also investigated by N-benzylideneaniline degradation under visible light irradiation, 30% degradation efficiency was achieved in 2 h. The mesoporous structure of TiO$_2$ offers more active sites for efficient adsorption of target organic molecules. Meanwhile, the up-conversion property and electron acceptor property of CQDs facilitate the usage of visible light and hinder the electron/hole recombination process, respectively. The synergistic effects of optical properties of CQDs and mesoporosity of TiO$_2$ lead to a remarkable visible light responsive photocatalyst. The CQDs/meso-Ti-450 composite has great potential as an environmentally friendly catalyst in visible light induced photocatalysis.

Acknowledgments

Appendix A. Supplementary data

Supplementary data associated with this article can be found, in the online version, at http://dx.doi.org/10.1016/j.apcatb.2016.01.070.

References

[1] G. Zu, J. Shen, W. Wang, L. Zou, Y. Lian, Z. Zhang, ACS Appl. Mater. Interfaces 7 (2015) 5400–5409.
[2] B.Y. Yu, S.-Y. Kwak, J. Mater. Chem. 22 (2012) 8345–8353.
[3] Y. Zhang, L. Jin, K. Sterling, Z. Luo, T. Jiang, R. Miao, C. Guild, S.L. Suib, Green Chem. 17 (2015) 3600–3608.
[4] L. Sun, W. Wu, S. Yang, J. Zhou, M. Hong, X. Xiao, F. Ren, C. Jiang, ACS Appl. Mater. Interfaces 6 (2014) 1113–1124.
[5] H. Li, R. Liu, Y. Liu, H. Huang, H. Yu, H. Ming, S. Lian, S.-T. Lee, Z. Kang, J. Mater. Chem. 22 (2012) 17470–17475.
[6] L. Xu, Y.L. Hu, C. Pelligra, C.H. Chen, L. Jin, H. Huang, S. Sithambaram, M. Aindow, R. Joesten, S.L. Suib, Chem. Mater. 21 (2009) 2875–2885.
[7] K. Nakata, A. Fujishima, J. Photochem. Photobiol. C Photochem. Rev. 13 (2012) 169–189.
[8] J.M. Macak, M. Zlamal, J. Krysa, P. Schmuki, Small 3 (2007) 300–304.
[9] S. Liu, J. Yu, M. Jaroniec, J. Am. Chem. Soc. 132 (2010) 11914–11916.
[10] S.G. Kumar, L.G. Devi, J. Phys. Chem. A 115 (2011) 13211–13241.
[11] H.C. Genuino, D.B. Hamal, Y. Fu, S.L. Suib, J. Phys. Chem. C 116 (2012) 14040–14051.
[12] H.R. Jafry, M.V. Liga, Q. Li, A.R. Barron, Environ. Sci. Technol. 45 (2011) 1563–1568.
[13] H. Zhang, X. Lv, Y. Li, Y. Wang, J. Li, ACS Nano 4 (2010) 380–386.
[14] D.C. Hurum, A.G. Agrios, K.A. Gray, T. Rajh, M.C. Thurnauer, J. Phys. Chem. B 107 (2003) 4545–4549.
[15] D.O. Scanlon, C.W. Dunnill, J. Buckeridge, S. a Shevlin, A.J. Logsdail, S.M. Woodley, C.R. a Catlow, M.J. Powell, R.G. Palgrave, I.P. Parkin, G.W. Watson, T.W. Keal, P. Sherwood, A. Walsh, A.a Sokol, Nat. Mater. 12 (2013) 798–801.
[16] S. Sakthivel, H. Kisch, Angew. Chem. Int. Ed. Engl. 42 (2003) 4908–4911.
[17] W. Ren, Z. Ai, F. Jia, L. Zhang, X. Fan, Z. Zou, Appl. Catal. B Environ. 69 (2007) 138–144.
[18] X. Chen, C. Burda, J. Am. Chem. Soc. 130 (2008) 5018–5019.
[19] Z. Luo, A.S. Poyraz, C. Kuo, R. Miao, Y. Meng, S. Chen, T. Jiang, C. Wenos, S.L. Suib, Chem. Mater. 27 (2015) 6–17.
[20] S. Zhuo, M. Shao, S.-T. Lee, ACS Nano 6 (2012) 1059–1064.
[21] W. Li, Z. Wu, J. Wang, A.A. Elzatahry, D. Zhao, Chem. Mater. 26 (2014) 287–298.
[22] T. Jiang, S. Du, T. Jafari, W. Zhong, Y. Sun, W. Song, Z. Luo, W. a. Hines, S.L. Suib, Appl. Catal. A Gen. 502 (2015) 105–113.
[23] N. Bao, Y. Li, Z. Wei, G. Yin, J. Niu, J. Phys. Chem. C 115 (2011) 5708–5719.
[24] H. Li, Z. Bian, J. Zhu, Y. Huo, H. Li, Y. Lu, J. Am. Chem. Soc. 129 (2007) 4538–4539.
[25] Y. Feng, L. Li, M. Ge, C. Guo, J. Wang, L. Liu, ACS Appl. Mater. Interfaces 2 (2010) 3134–3140.
[26] T. Zhu, J. Li, Q. Wu, ACS Appl. Mater. Interfaces 3 (2011) 3448–3453.
[27] A.S. Poyraz, C. Kuo, S. Biswas, S.L. Suib, Nat. Commun. 4 (2013) 2952–2961.
[28] T. Jiang, A.S. Poyraz, A. Iyer, Y. Zhang, Z. Luo, W. Zhong, R. Miao, A.M. El-Sawy, C.J. Guild, Y. Sun, D.a Kriz, S.L. Suib, J. Phys. Chem. C 119 (2015) 10454–10468.
[29] C.-H. Kuo, I.M. Mosa, A.S. Poyraz, S. Biswas, A.M. El-Sawy, W. Song, Z. Luo, S.-Y. Chen, J.F. Rusling, J. He, S.L. Suib, ACS Catal. 5 (2015) 1693–1699.
[30] N.D. Wasalathanthri, A.S. Poyraz, S. Biswas, Y. Meng, C.-H. Kuo, D.a. Kriz, S.L. Suib, J. Phys. Chem. C 119 (2015) 1473–1482.
[31] W. Song, A.S. Poyraz, Y. Meng, Z. Ren, S. Chen, S.L. Suib, Chem. Mater. 26 (2014) 4629–4639.
[32] Y. Yao, G. Li, S. Ciston, R.M. Lueptow, Environ. Sci. Technol. 42 (2008) 4952–4957.
[33] L.-W. Zhang, H.-B. Fu, Y.-F. Zhu, Adv. Funct. Mater. 18 (2008) 2180–2189.
[34] S. Kong, Z. Jin, H. Liu, Y. Wang, J. Phys. Chem. C 118 (2014) 25355–25364.
[35] P. Zhang, S. Rogelj, K. Nguyen, D. Wheeler, J. Am. Chem. Soc. 128 (2006) 12410–12411.
[36] J. Boyer, F. Vetrone, L.A. Cuccia, J.A. Capobianco, Q.C. Hb, I. National, D. Recherche, J. Am. Chem. Soc. 128 (2006) 7444–7445.
[37] J. Boyer, L.A. Cuccia, J.A. Capobianco, Nano Lett. 7 (2007) 847–852.
[38] Z. Chen, H. Chen, H. Hu, M. Yu, F. Li, Q. Zhang, Z. Zhou, T. Yi, C. Huang, J. Am. Chem. Soc. 130 (2008) 3023–3029.
[39] Y. Han, H. Huang, H. Zhang, Y. Liu, X. Han, R. Liu, H. Li, Z. Kang, ACS Catal. 4 (2014) 781–787.
[40] H. Li, Z. Kang, Y. Liu, S.-T. Lee, J. Mater. Chem. 22 (2012) 24230–24253.
[41] X. Michalet, F.F. Pinaud, L.a. Bentolila, J.M. Tsay, S. Doose, J.J. Li, G. Sundaresan, a M. Wu, S.S. Gambhir, S. Weiss, Science 307 (2005) 538–544.
[42] H. Xu, R. Miao, Z. Fang, X. Zhong, Anal. Chim. Acta 687 (2011) 82–88.
[43] Y. Sun, B. Zhou, Y. Lin, W. Wang, K.A.S. Fernando, P. Pathak, M.J. Meziani, B.A. Harruff, X. Wang, H. Wang, P.G. Luo, H. Yang, M.E. Kose, B. Chen, L.M. Veca, S. Xie, S. Carolina, J. Am. Chem. Soc. 128 (2006) 7756–7757.
[44] P. Yu, X. Wen, Y.-R. Toh, J. Tang, J. Phys. Chem. C 116 (2012) 25552–25557.
[45] X. Yu, J. Liu, Y. Yu, S. Zuo, B. Li, Carbon N. Y. 68 (2014) 718–724.
[46] Y. Zhu, X. Ji, C. Pan, Q. Sun, W. Song, L. Fang, Q. Chen, C.E. Banks, Energy Environ. Sci. 6 (2013) 3665–3675.
[47] J. Zhou, C. Booker, R. Li, X. Zhou, T.K. Sham, X. Sun, Z. Ding, J. Am. Chem. Soc. 129 (2007) 744–745.
[48] S.T. Yang, L. Cao, P.G. Luo, F. Lu, X. Wang, H. Wang, M.J. Meziani, Y. Liu, G. Qi, Y.P. Sun, J. Am. Chem. Soc. 131 (2009) 11308–11309.
[49] H. Liu, T. Ye, C. Mao, Angew. Chem. Int. Ed. 46 (2007) 6473–6475.
[50] D. Pan, J. Zhang, Z. Li, M. Wu, Adv. Mater. 22 (2010) 734–738.
[51] N. Gong, H. Wang, S. Li, Y. Deng, X. Chen, L. Ye, W. Gu, Langmuir 30 (2014) 10933–10939.
[52] H. Li, X. He, Z. Kang, H. Huang, Y. Liu, J. Liu, S. Lian, C.H.A. Tsang, X. Yang, S.-T. Lee, Angew. Chem. Int. Ed. 49 (2010) 4430–4434.
[53] L. Cao, X. Wang, M.J. Meziani, F. Lu, H. Wang, P.G. Luo, Y. Lin, B.a. Harruff, L.M. Veca, D. Murray, S.-Y. Xie, Y.-P. Sun, J. Am. Chem. Soc. 129 (2007) 11318–11319.
[54] H. Nie, M. Li, Q. Li, S. Liang, Y. Tan, L. Sheng, W. Shi, S.X.-A. Zhang, Chem. Mater. 26 (2014) 3104–3112.
[55] D.A. Links, Phys. Chem. Chem. Phys. 14 (2012) 7360–7366.
[56] Z. Yang, M. Wang, M. Yong, Y. Wong, X. Zhang, Chem. Commun. 47 (2011) 11615–11617.
[57] H. Ming, Z. Ma, Y. Liu, K. Pan, H. Yu, F. Wang, Z. Kang, Dalton Trans. 41 (2012) 9526–9531.
[58] H. Search, C. Journals, A. Contact, M. Iopscience, Reports Prog. Phys. 62 (1999) 1573–1659 (I.P. Address).
[59] S. Storck, H. Bretinger, W.F. Maier, Appl. Catal. A Gen. 174 (1998) 137–146.
[60] J. Wang, C.-F. Wang, S. Chen, Angew. Chem. Int. Ed. 51 (2012) 9297–9301.
[61] L. Zeng, Z. Lu, M. Li, J. Yang, W. Song, D. Zeng, C. Xie, Appl. Catal. B Environ. 183 (2016) 308–316.
[62] J. Pan, Y. Sheng, J. Zhang, J. Wei, P. Huang, X. Zhang, B. Feng, J. Mater. Chem. A 2 (2014) 18082–18086.
[63] A.S. Poyraz, W. Song, D. Kriz, C. Kuo, M.S. Seraji, S.L. Suib, ACS Appl. Mater. Interfaces 6 (2014) 2–7.
[64] H. Li, X. He, Y. Liu, H. Huang, S. Lian, S.T. Lee, Z. Kang, Carbon N. Y. 49 (2011) 605–609.
[65] O. Kozák, K.K.R. Datta, M. Greplová, V. Ranc, J. Kašlík, R. Zbořil, J. Phys. Chem. C 117 (2013) 24991–24996.
[66] X. Wen, P. Yu, Y.-R. Toh, X. Ma, J. Tang, Chem. Commun. (Camb). 50 (2014) 4703–4706.
[67] H. Wang, Z. Wei, H. Matsui, S. Zhou, J. Mater. Chem. A 2 (2014) 15740–15745.

[68] H. Zhang, H. Huang, H. Ming, H. Li, L. Zhang, Y. Liu, Z. Kang, J. Mater. Chem. 22 (2012) 10501–10506.
[69] L. Zhang, J. Lian, L. Wu, Z. Duan, J. Jiang, L. Zhao, Langmuir 30 (2014) 7006–7013.
[70] H. Adamu, P. Dubey, J.A. Anderson, Chem. Eng. J. 284 (2016) 380–388.
[71] X. Yan, T. Ohno, K. Nishijima, R. Abe, B. Ohtani, Chem. Phys. Lett. 429 (2006) 606–610.
[72] B. Ohtani, J. Photochem. Photobiol. C Photochem. Rev. 11 (2010) 157–178.